3D micro-mechanical modelling of orthogonal cutting of UD-CFRP using smoothed particle hydrodynamics and finite element methods

Abena, Alessandro; Essa, Khamis

DOI:
10.1016/j.compstruct.2019.03.037

Document Version
Peer reviewed version

Citation for published version (Harvard):
Abena, A & Essa, K 2019, '3D micro-mechanical modelling of orthogonal cutting of UD-CFRP using smoothed particle hydrodynamics and finite element methods', *Composite Structures*, vol. 218, pp. 174-192. https://doi.org/10.1016/j.compstruct.2019.03.037

3D micro-mechanical modelling of orthogonal cutting of UD-CFRP using Smoothed Particle Hydrodynamics and Finite Element methods

Alessandro Abena*, Khamis Essa

Department of Mechanical Engineering, School of Engineering, University of Birmingham, Birmingham, B15 2TT, U.K.

Abstract

FE models of orthogonal cutting of FRP composites are usually used implementing element deletion when the failure condition has been reached. This typically results in loss of contact between tool and workpiece during cutting leading to very poor thrust force prediction. In this study, a comprehensive three-dimensional numerical model of orthogonal cutting of UD-CFRP employing the SPH method at the micro-scale level is developed for different fibre orientations (θ=0°,45°,90°,135°). Results are compared with those obtained by a FEM model and against experimental findings. Results show that the SPH method is able to improve prediction of cutting force (∼30% at θ=0°) and thrust force (∼30% at θ=90°,135°), showing also a chip formation mechanism closer to that experimentally observed. In addition, the developed approach allows simulating the bouncing back, that for θ=0° results equal to the cutting edge radius (∼5 μm), as expected from the literature, and calculating the actual depth of cut.

Keywords: Orthogonal cutting, Carbon Fibre Reinforced Plastic Composites (CFRP), Bouncing back, Smoothed Particle Hydrodynamics (SPH), Finite Element Method (FEM)

*Corresponding author

Email address: a.abena@bham.ac.uk (Alessandro Abena)

1. Introduction

Fibre reinforced plastic (FRP) composite materials are increasingly being used in high performance applications within various industrial sectors due to their superior properties in terms of specific strength/stiffness, corrosion resistance, damage tolerance and resistance to fatigue; as well as thermal and acoustic insulation power, when compared with conventional material/alloys.

During production, machining operations are required for the removal of excess material to meet dimensional tolerances or for producing holes for assembly. The inhomogeneous and anisotropic nature of composite materials still represents a challenge in terms of machinability. Defects can arise during machining in each phase of the material, hence involving the fibre, matrix, and fibre-matrix interface. The presence of such flaws can compromise surface integrity and lead to poor component in-service performance. The importance of minimizing/eliminating workpiece damage following machining, has led industries and researchers to investigate these processes.

Numerical models seem to be the most flexible tool for studying the machining of composite materials. In fact, they can provide detailed information at different scale levels (from the macro-scale to the micro-scale), that could be difficult to obtain using different approaches (experimental, analytical, and empirical). However, the numerical approach still needs to be validated against experimental results.

Usually, the orthogonal cutting is used to study the removal mechanism when machining composite materials. Several chip formation mechanisms have been identified depending on fibre orientation (θ) and tool rake angle (α) [1–3], as it is shown in Figure 1. For fibre orientation θ=0° and positive rake angle, the tool progression causes fibre-matrix interface damage with consequent fibre failure due to bending (Type I). For negative rake angle, fibre failure due to buckling takes place (Type II). For $0°<\theta<75°$ and independently from the rake angle, the chip formation mechanism is caused by compression induced shear across the fibre axis, and shear fracture of fibre-matrix interface along the fibre direction (Type III). The chip formation mechanism for $75°<\theta<90°$ is characterized by compression induced fracture perpendicular to the fibre axis, and interface fracture due to shear along the fibre-matrix interface (Type IV). For $\theta>90°$ the chip formation mechanism involves: considerable out-of-plane displacement; intra-laminar shear at the fibre-matrix interface; and bending deformations due to compression exerted by the tool, which leads to fibre and matrix failure usually below the cut-

ting plane (Type V). The chip formation mechanisms described are typical of machining carried out using a sharp cutting edge (nose radius of a few micrometer). When machining with a round cutting edge, a different chip formation mechanism has been observed for θ=90° [1, 4] where the tool is not able to cut the fibre at the contact point, but it exerts compression loading on the sample causing fibre bending and failure below the cutting plane. In addition, when machining with a round cutting edge, it is possible to identify a part of the workpiece which is compressed under the tool. After the tool has passed, the material exhibits an elastic recovery. The amount of spring back the material undergoes is called bouncing back.

Over the years, simulation of orthogonal cutting of unidirectional fibre reinforced plastic (UD-FRP) composite has been continuously improved in an attempt to make it as accurate as possible. In particular, models implementing the macro-mechanical approach have been widely used. It involves representing the composite workpiece as an equivalent homogeneous material (EHM), whose properties can be derived by means the rule of mixtures [5] and provides only general information on the chip formation mechanism [6–9]. In contrast, the recently developed micro-mechanical approach accounts for each material phase separately [10–12], thus enabling more detailed simulation/analysis of material deformation and defect formation during machining. The micro-mechanical model represents a powerful approach to analysing processes at the microscopic level. However, it is still computationally prohibitive for simulating machining operations involving a large amount of material, such as drilling, where the EHM approach has been used [13–15]. This led several researchers to develop a meso-scale formulation [16–19]. Here, the microscopic model is implemented in the vicinity of the tool, while the EHM approach is used for the rest of the model, in order to provide the necessary stiffness while minimising the computational cost.

Most of simulations implementing micro-mechanical or meso-scale approaches are two-dimensional in order to reduce the computational cost [11, 17, 18]. A three-dimensional model obtained by mean extrusion of a two-dimensional model in direction orthogonal to the cutting speed was developed by Abena *et al.* [20] and by Chennakesavelu [21], while more realistic three-dimensional models implementing cylindrical fibres are few [22, 23].

Models for simulating machining of composite materials usually employ the finite element method. In it, elements are deleted from the analysis when the failure condition has been reached. While cutting force is usually in good agreement, thrust force is generally underestimated. Indeed, a signi-

ficant underestimation of thrust force has been observed and highlighted in several works [16, 22, 24]. The numerical thrust force values can be one order of magnitude lower than the experimental values, as shown by Calzada *et al.* [16]. This underestimation has been attributed to the failure and subsequent deletion of elements during the analysis along the cutting path; thereby causing a relaxation in the force component due to the loss of contact between the tool and the workpiece [16, 24].

For this reason the current work aims to reduce/eliminate the significant underestimation of predicted thrust force employing the Smoothed Particle Hydrodynamics (SPH) method, which is part of the mesh-free methods family. The SPH method can handle large deformations and material opening due to tool action without element deletion and it has been successfully used for simulating orthogonal cutting in metals [25–30]. Degradation of material properties after material failure allows particles to separate. In this way, non-physical material loss observed in FE models will be avoided, ensuring tool-workpiece contact during the whole cutting process, improving the thrust force. In addition, implementation of SPH method will allow to simulate and study the amount of elastic recovery after the tool has passed (bouncing back). This is extremely important since bouncing back affects the depth of cut obtained after machining and the thrust force [3, 31]. The contribution to the thrust force is due to the pressure the workpiece applies on the tool clearance face due to the elastic recovery after cut. For this purpose, simulation of orthogonal cutting of unidirectional carbon fibre reinforced plastic (UD-CFRP) composite at different fibre orientations (θ=0°,45°,90°,135°) employing the SPH method will be presented and results will be compared with those obtained using the FE method and against experimental findings.

2. Numerical modelling of the orthogonal cutting of UD-CFRP

Simulation of the orthogonal cutting of UD-CFRP will be carried out implementing two numerical methods: finite element analysis and smoothed particle hydrodynamics method. Since the FE method is usually used for modelling machining of composites, models based on FE analysis will be used to assess improvement when using the SPH method. Development of both FE and SPH models is described in the following.

2.1. FEM modelling

A FE method was employed for modelling the orthogonal cutting of UD-CFRP in Abaqus/Explicit. In particular, a three-dimensional finite element model implementing cylindrical fibres was developed using a meso-scale approach to simulate the composite material, similarly to Abena *et al.* [20] work. Hence, a micro-mechanical approach was implemented in the area close to the tool tip, where the cut takes place, allowing to analyse the chip formation mechanism through single phases, providing detailed information on material deformation and failure mechanism during cutting. In order to reduce the computational cost, the composite was simulated as an equivalent homogeneous material (EHM) far from the cutting area. Further computational cost reduction was achieved modelling half of the fibres' geometry, assuming the symmetry. A schematic of the FEM model and of the boundary conditions applied in the case of fibre orientation θ=90° is reported in Figure 2. The depth of cut set in the model was 15 μm, and a cutting velocity boundary condition was assigned to the tool, realising a dynamic explicit analysis. For fibre orientation θ=0°, due to the small depth of cut a model implementing three fibres was developed. However, a fibre length of 200 μm along the cutting direction was considered in order to eventually accommodate a fibre failure due to bending, which is typical when machining at fibre angle θ=0° and positive rake angles. Below them, an EHM phase was positioned in order to introduce the necessary stiffness.

The epoxy matrix was implemented according to a static compressive stress-strain curve at room temperature and the element in the model was considered failed when the Von Mises stress reaches the ultimate stress level, while the carbon fibres were simulated as transversely isotropic and perfectly elastic to failure with failure criterion based on the maximum principal stress. Both failure criteria have been already used in the literature to study the orthogonal cutting on FRPs' material [17, 18, 24]. The material properties are reported in Table 1.

Contact conditions were implemented through general contact algorithm, where the penalty method was used to enforce the contact constraint between surfaces. The contact property was defined in terms of Coulomb model considering a constant friction coefficient equal to 0.3 for all fibre orientations, as suggested by Venu Gopala Rao *et al.* [17].

About the modelling of the cohesive zone, the novel approach developed by Abena *et al.* [20] was implemented to avoid excessive deformation of cohesive elements, which usually leads to analysis failure, and obtain a good

representation and description of the cohesive behaviour during the analysis. This approach utilises zero thickness cohesive elements based on traction-separation law, where coupling of traction and shear is considered for damage initiation and failure. In addition, failure due to connectivity is implemented by means of a user-defined field subroutine (VUSDFLD) so that the cohesive element fails when one of the surrounding elements (matrix or fibre), at which it is connected, fails. Tie constraint was implemented between the EHM and micro-mechanical zone, and also between adjacent phases (matrix, fibre and cohesive).

The mesh in the micro-mechanical area was realized by employing 3D Stress Hex elements and setting the mesh seed on the edges equal to 1 μm. In order to reduce the computational cost of the analysis, coarse mesh was used in the EHM zone with elements having a maximum length of 10 μm in the x-y plane far from the cutting area.

Further details on the FEM model can be found in Abena [1] work.

2.2. SPH modelling

A three-dimensional model with cylindrical fibres was developed implementing the SPH method in Abaqus software, as shown in Figure 3. The depth of cut set in the model was 15 μm, and a cutting velocity boundary condition was assigned to the tool, realising a dynamic explicit analysis. In order to reduce the computational cost, half geometry for the fibres was considered, assuming the symmetry as for the FE model. The model was not entirely composed of SPH elements; in fact the finite element method was used for the EHM phase. The boundary conditions were the same as applied in the models using the FE method. Tie constraint was applied between the SPH matrix and the EHM phase. Since SPH particles can undergo large displacements, even flying away from the cutting area in case damage is experienced, the imposition of the condition of symmetry on the SPH elements is not sufficient. For this reason, two rigid surfaces were positioned in the model on both sides, avoiding particles moving in z direction out from the simulated strip. Contact with no friction was implemented between particles and rigid surfaces. Particles were positioned in the model with a relative distance of 1 μm, in order to reduce as much as possible any difference with the models developed using the FE method where a mesh seed of 1 μm was used. No condition was needed to be set between the fibres and matrix particles. Unfortunately, unlike the FEM, no cohesive model can be implemented when

the SPH method is used. Therefore, information on the fibre-matrix interface cannot be obtained.

In order to simulate interaction between parts having different material models using the SPH method, an user subroutine needed to be developed as described in detail below.

Implementation of a VUMAT subroutine for the SPH model. The main limitation when using the SPH method in Abaqus exists in the inability to simulate the interaction between two or more parts modelled with that method, to which different material models have been assigned. In the present model, two different phases based on the SPH method are implemented: fibre and matrix. Hence, it is of fundamental importance to overcome this limitation. To this end, a user subroutine has been developed, in which material models for fibre and matrix have been implemented. In fact, fibre and matrix have been developed in the same part in Abaqus/CAE. Afterwards, knowing the ID number of particles belonging to each phase, different properties and constitutive behaviours have been assigned to each particle using a field variable in a VUMAT subroutine to identify fibre and matrix. Using the described method, a unique material card can be used in the analysis, making possible the simulation of the contact between fibre and matrix.

In order to compare results obtained using the SPH and the FE method, the constitutive behaviour for each phase coded in the VUMAT has to be the same as implemented using Abaqus/CAE in Section 2.1. However, for each material model, the material damage also needs to be coded together with post-failure behaviour, since elements are not deleted in the SPH method.

Matrix material has been coded having an elasto-plastic behaviour, with the plastic region defined by means of Von Mises yield criterion, and isotropic hardening.

The general approach to simulate material damage that can be used for the matrix phase in Abaqus is reported in Figure 4(a). The elastic behaviour identified by the Young's modulus E, and by the yield stress σ_0 can be recognised, followed by the plastic behaviour. When material damage is introduced in the material model, σ_{y0} and $\bar{\epsilon}_0^{pl}$ identify the damage initiation condition, representing the yield stress and the equivalent plastic strain at the onset of damage, respectively. In order to simulate the damage evolution during the analysis, a damage variable $0 \leq D \leq 1$ has to be considered, simulating the damage through material stiffness degradation. At the damage initiation point, the damage variable assumes value $D=0$. It rises with

the increase of damage experienced by the element till it reaches the unitary value, at which the element loses its load-carry capacity and is deleted from the simulation. The failure condition is identified by the equivalent plastic strain at failure $\bar{\epsilon}_f^{pl}$.

In the FEM model, no damage evolution is set, with the element failing once the Von Mises stress reaches the ultimate stress level (Figure 4(b)).

In order to obtain the same behaviour using the VUMAT subroutine, the condition reported in Equation (1) [32] has been implemented to identify damage initiation:

$$\omega_D = \int \frac{d\bar{\epsilon}^{pl}}{\bar{\epsilon}_D^{pl}} = 1 \tag{1}$$

where ω_D is a state variable increasing with the plastic deformation; and $\bar{\epsilon}_D^{pl}$ represents the equivalent plastic strain at the onset of damage. No damage evolution has been considered after damage initiation. However, differently from the FEM, the element is not deleted from the analysis. The material stiffness is instantaneously degraded considering a value of the damage variable of D=0.8, which has been kept constant over all the analysis after the damage initiation condition was verified in the element. The value of the damage variable (D=0.8) was obtained by means of a parametric study aiming to match the experimental cutting force and thrust force values. The constitutive behaviour can be represented as reported in Figure 4(c).

As for the FEM model, the fibre has been simulated in the VUMAT as transversely isotropic and perfectly elastic until damage initiation. The latter is represented by the maximum principal stress criterion. It is verified when the maximum compressive/tensile principal stress in an element exceeds the fibre compressive/tensile strength limit. When this happens, the element is deleted by the analysis in the FEM. Differently, material stiffness degradation has been implemented for the SPH method. In particular, the fibre constitutive model with the associated stiffness matrix is reported in Equation (2) [32–34]:

$$\begin{bmatrix}\sigma_{11}\\ \sigma_{22}\\ \sigma_{33}\\ \tau_{12}\\ \tau_{23}\\ \tau_{13}\end{bmatrix} = \begin{bmatrix}C_{11} & C_{12} & C_{13} & 0 & 0 & 0\\ C_{21} & C_{22} & C_{23} & 0 & 0 & 0\\ C_{31} & C_{32} & C_{33} & 0 & 0 & 0\\ 0 & 0 & 0 & C_{44} & 0 & 0\\ 0 & 0 & 0 & 0 & C_{55} & 0\\ 0 & 0 & 0 & 0 & 0 & C_{66}\end{bmatrix} \begin{bmatrix}\epsilon_{11}\\ \epsilon_{22}\\ \epsilon_{33}\\ \gamma_{12}\\ \gamma_{23}\\ \gamma_{13}\end{bmatrix}$$

$$\begin{aligned}
&N = 1 - \nu_{12}\nu_{21} - \nu_{23}\nu_{32} - \nu_{31}\nu_{13} - 2\nu_{21}\nu_{32}\nu_{13}\\
&C_{11} = (1 - \nu_{23}\nu_{32})E_1/N \qquad C_{12} = (\nu_{12} + \nu_{13}\nu_{32})E_2/N\\
&C_{13} = (\nu_{13} + \nu_{12}\nu_{32})E_3/N \quad C_{21} = (\nu_{21} + \nu_{31}\nu_{23})E_1/N\\
&C_{22} = (1 - \nu_{13}\nu_{31})E_2/N \qquad C_{23} = (\nu_{23} + \nu_{13}\nu_{21})E_3/N\\
&C_{31} = (\nu_{31} + \nu_{21}\nu_{23})E_1/N \quad C_{32} = (\nu_{32} + \nu_{31}\nu_{12})E_2/N\\
&C_{33} = (1 - \nu_{12}\nu_{21})E_3/N \qquad C_{44} = 2G_{12} \qquad C_{55} = 2G_{23} \qquad C_{66} = 2G_{13}\\
&E_1 = E_1^{DS}(1 - d_1) \qquad E_2 = E_2^{DS}(1 - d_2) \qquad E_3 = E_3^{DS}(1 - d_3)\\
&\nu_{12} = \nu_{12}^{DS}(1 - d_1) \qquad \nu_{21} = \nu_{21}^{DS}(1 - d_2) \qquad \nu_{13} = \nu_{13}^{DS}(1 - d_1)\\
&\nu_{31} = \nu_{31}^{DS}(1 - d_3) \qquad \nu_{23} = \nu_{23}^{DS}(1 - d_2) \qquad \nu_{32} = \nu_{32}^{DS}(1 - d_3)\\
&G_{12} = G_{12}^{DS}(1 - d_{s12}) \qquad G_{13} = G_{13}^{DS}(1 - d_{s13}) \qquad G_{23} = G_{23}^{DS}(1 - d_{s23})\\
&d_{s12} = 1 - (1 - d_1)(1 - d_2) \qquad d_{s13} = 1 - (1 - d_1)(1 - d_3)\\
&d_{s23} = 1 - (1 - d_2)(1 - d_3)
\end{aligned} \tag{2}$$

where the superscript DS stands for data-sheet, i.e. terms associated with this symbol represent the material properties without damage.

Three damage variables have also been introduced: d_1, d_2, d_3. The former is linked with the damage along the fibre direction 1, while the other two govern the damage in the plane of isotropy 2-3. Hence, d_2 and d_3 have the same value. The damage variables can be implemented straightforwardly to calculate the damaged Young's modulus for each direction; and used to calculate the damaged Poisson's ratio. In fact, even for the damaged material, Equation (3) has to be satisfied [34]:

$$\frac{\nu_{ij}}{E_i} = \frac{\nu_{ji}}{E_j} \tag{3}$$

In addition, d_{s12}, d_{s13}, d_{s23} represent the damage variables to shear in the planes 1-2, 1-3, and in the plane of isotropy 2-3, respectively. Similarly

to what is reported in the Abaqus manual on damage and failure for fibre-reinforced composites [32], the generic shear damage variable d_{sij} is calculated as a function of the damage variables in direction i and j, i.e. d_i and d_j, respectively.

The damage variables' values are set to zero if the damage initiation condition has not been satisfied ($d_1 = d_2 = d_3 = 0$). Otherwise, material degradation takes place instantaneously, without damage evolution, and damage variables are set directly to the maximum and final values considered: $d_1 = 0.4$, $d_2 = 0.8$, $d_3 = 0.8$. The values of the damage variables (d_1, d_2, d_3) were obtained by means of a parametric study aiming to match the experimental cutting force and thrust force values.

Material properties implemented for each phase in the SPH model are the same as those used in the FEM model (Table 1).

Further details on the SPH model can be found in Abena [1] work.

3. Validation of modelling results

Models developed were validated against orthogonal cutting experiment realised by Calzada *et al.* [16]. A micro-machining of unidirectional CFRP was carried out considering different fibre orientation (θ=0°,45°,90°,135°), where the fibre angle is defined as shown in Figure 5a. Tool geometry and machining parameters used, in terms of cutting speed and depth of cut, are reported in Table 2. For each fibre orientation cutting force and thrust force were measured by means of an Kistler 9018 triaxial load cell embedded into the tool. In addition, a Phantom v.7.0 high-speed camera was used to observe and study the chip formation mechanism. During machining the tool was held stationary while the workpiece was moved along the cutting direction. A schematic of the experiment setup is shown in Figure 5b. This experiment has been chosen as reference for model validation because it takes place at the micro-scale level, helping in reducing the computational cost of the analysis. In fact, since it is a micro-machining, the amount of material involved in the cut is contained around the cutting zone allowing to model a smaller part of the workpiece containing the computational cost.

4. Results and discussion

Results obtained using FE method and SPH method are presented and discussed in this section. In particular, a comparison is carried out looking

at the chip formation mechanism, damage, type and morphology of the chip, cutting force and thrust force for each fibre orientation. In addition, analysis of cohesive element behaviour has been carried out for FE model. Numerical results are also compared with experimental findings to assess the differences between two approaches used.

4.1. Chip formation mechanism and damage at various fibre orientations

4.1.1. FE model results

Fibre orientation θ=0°. Configuration of the model during cutting is reported in Figure 6. During tool advancement matrix crushing and fibre failure due to compression is observed, with curling chip formed by a thin matrix material, once the fibre elements are deleted. This material removal mechanism differs from the experimentally observed Type I [16] and expected from the literature [35, 36], where fibre failure is due to bending ahead of the cutting tool. This is due to deletion of elements once the failure criterion has been reached.

Variable PEEQ, provided as output in Abaqus software, represents the equivalent plastic strain, i.e. the amount of permanent/non recoverable strain accumulated in the machined workpiece. This variable was chosen to analyse the matrix condition after machining (Figure 7(a)). Plastic deformation remains close to the cutting plane, reaching a few micrometers in depth.

For analysing cohesive elements, Abaqus software provides as output the SDEG variable. It represents the overall value of the scalar damage in the cohesive elements. Its value varies from zero to one. A value equal to zero means that the cohesive element has not experienced damage yet. The value of the SDEG variable increases with the increment of damage accumulated in the cohesive element. When the unitary value is reached, the cohesive element fails and it is deleted from the analysis. Therefore, a value of SDEG variable close to unity means an imminent failure of the cohesive element. The SDEG variable is used to study the cohesive behaviour during machining (Figure 7(b)). Cohesive elements experience damage ahead of the tool. However, they fail only when they come close to the tool, due to surrounding element failure. Finally, small amount of damage is visible for cohesive elements below the machined surface.

Fibre orientation θ=45°. Configuration of the model during cutting is reported in Figure 8, where the chip formation mechanism can be observed. Due to tool advancement, a crack propagates from the contact point across

the fibre, orthogonally to the fibre axis (Figure 8(a)). Further tool displacement causes a fibre failure due to compression, as observed in the experiment [16], with fibre release along its axis (Figure 8(b)). In the meantime, matrix crushing takes place between two consecutive fibres and at the contact point with the tool.

Variable PEEQ was considered to analyse the matrix condition after machining (Figure 9(a)). It is possible to observe that plastic deformations extend below the cutting plane, reaching a maximum depth ($\sim$4.2 μm) between two consecutive fibres. Plastic deformations are also visible ahead of the cutting tool, which start from the tool tip and propagate along the fibre axis due to the shear.

The cohesive elements' behaviour during cutting is shown in Figure 9(b) and Figure 10. Due to tool advancement, fibres undergo displacement along their axis. Hence, cohesive elements experience shear and normal deformation until failure, which is mainly due to the former.

The chip formation mechanism predicted by the FEM model agrees well with Type III in literature [2, 35].

Fibre orientation θ=90°. The chip formation mechanism is shown in Figure 11. Crack formation takes place at the contact point with the tool. It propagates in a direction orthogonal to the fibre axis, cutting the fibre into two parts, as observed by Calzada *et al.* [16]. Due to tool advancement, the upper part of the cracked fibre is lifted and compressed against the next fibre, experiencing further compression failure and forming the chip. No bending failure, usually taking place below the cutting plane, was observed, in agreement with experimental findings [16]. This behaviour represents the expected chip formation mechanism, typical of Type IV [2, 36].

Matrix failure is due to compression. A crack extending vertically for $\sim$10 μm corresponding to the third fibre can be observed in Figure 12(a). The PEEQ variable shows how plastic deformations are experienced by the matrix far below the trim plane ($\sim$30 μm) after machining and ahead of the cutting tool. However, elements representing the matrix fail mainly above the cutting plane.

The cohesive elements' damage after machining is reported in Figure 12(b). Damage depth reaches almost the end of the finite element model, hence having a depth of about 100 μm. However, the variable SDEG generally does not reach the unitary value, so debonding is not generated.

During machining, cohesive elements undergo shear. However, cohesive

elements' failure is caused by surrounding element failure. This is also the cause of the vertical crack taking place in cohesive elements at the matrix failure location below the cutting plane.

Fibre orientation θ=135°. The chip formation mechanism is shown in Figure 13. The cutting tool engages the fibre causing bending deformation until failure, as expected from experimental observation [16] and represents Type V removal mechanism reported in the literature [3, 37]. Fibre fracture occurs a few micrometres below the trim plane in the model, while in the experiment fibre length in the chip has been found about 50 μm-80 μm, suggesting a fibre fracture due to bending deeper below the cutting plane. Due to matrix compression failure, two consecutive fibres come into contact. In particular, the upper part of the fractured fibre pushes against the top part of the next fibre, causing a crack formation at a higher position. Hence, the crack propagates orthogonally to the fibres' axis towards the free surface of the sample. At the end of the analysis a crack is visible below the cutting plane in the fourth fibre. It is due to further bending caused by tool advancement in the already fractured fibre.

Due to fibre bending and to the pushing action of the tool, debonding takes place at the fibre-matrix interface, as shown in Figure 14. The cohesive elements fail sequentially with fibre bending increase, with damage extending deeper in the workpiece. Information on damage experienced by cohesive elements is reported in Figure 15(b). Damage extends along the fibre direction deep in the workpiece ∼48 μm below the cutting plane and a maximum debonding length of ∼17 μm was observed.

Matrix failure and plastic deformations after machining are shown in Figure 15(a). Matrix failure due to compression takes place between two consecutive fibres above the cutting plane. Due to fibre bending, a region where the matrix experiences tensile failure is visible below the cutting plane, generating a crack that penetrates deep in the workpiece (∼12 μm below the cutting plane).

4.1.2. SPH model results

Fibre orientation θ=0°. The deformed configuration of the model during cutting is reported in Figure 16. Abaqus software allows to assign different properties and constitutive behaviours to each particle depending on the phase that the particle represents in the model, i.e. fibre or matrix. As already reported in the description of the development of the SPH model,

the assignment of properties and constitutive behaviours to each particle was realised using a field variable (FV1) in a VUMAT subroutine. Properties and constitutive behaviours of matrix and fibre phases were identified by a value of the field variable (FV1) equal to zero and one, respectively. Therefore, the field variable FV1 provided in output by Abaqus software can also be used to visually distinguish fibres (FV1=1, red colour) from matrix (FV1=0, blue colour) in the simulation results (Figure 16).

In Figure 16 it is possible to observe that the absence of element deletion during the analysis totally changes the chip formation mechanism when compared with the FEM model (Figure 6). In particular, when the SPH method is employed, the bouncing back is observed during cutting due to the elastic recovery of the material after the tool has passed. In fact, the contact between the tool clearance face and the workpiece machined surface is clearly visible. This was not possible to detect in the FEM model due to the deletion of failed elements and represents an advantage of the SPH method, which shows a material behaviour closer to that usually observed during cutting of CFRP.

The tool causes fibre and matrix compression in the direction of the fibre axis during advancement, with consequent material damage around the tool-workpiece contact area. Differently from the FEM model, elements are not deleted from the analysis, but they experience degradation of the material properties. Hence, the damaged material cannot leave the cutting zone, as it is entrapped between the tool and the upper part of the material which is still not affected by damage. The damaged area expands with further tool advancement and a crack propagates horizontally ahead of it, affecting the elements located on the fibre-matrix border. In addition, the damaged material helps in transferring the tool action to the undamaged elements, favouring material opening. During crack propagation fibre bending takes place. When the crack reaches a length of $\sim$30 μm, it suddenly changes direction, moving through the fibre towards the free surface of the sample. In addition, the crack also moves through the matrix at the same time. When it reaches the free surface, the chip, composed of the cut fibre and matrix, is released and the process repeats again. Differently, in the FEM model a thin curl chip was formed by a small amount of matrix material located on the upper free edge of the sample. Almost the totality of the material in front of the tool, that was supposed to form the chip, was deleted from the analysis due to failure. This represents a non realistic behaviour, while that observed in the SPH model is closer to that observed by Calzada *et al.* [16]

and representative of Type I chip formation mechanism.

When writing a subroutine, Abaqus software allows the user to define solution-dependent state variables (SDVs). It is possible to associate to a solution-dependent state variable any quantity calculated in the subroutine, which will be stored and written in the results file and therefore available as output at the end of the simulation. For material model implementation the VUMAT subroutine was used in this work, and solution-dependent state variables were implemented to make variables of interest defined and calculated in the subroutine available in the results of the simulation.

The solution-dependent state variable SDV13 was used to store the damage experienced by the material, which is shown in Figure 17. The variable SDV13 assumes value equal to zero for particles that have not experienced damage yet and one for damaged particles, i.e. particles for which the material stiffness has been degraded to simulate damage. The damage extension tends to reach the EHM phase ($\sim$12 μm below the cutting plane). The damaged material can also be observed until $\sim$8 μm ahead of the cutting tool. Considering the fibres (Figure 17(a)), damage is mainly concentrated along the crack propagation path in the external fibre, which allows the formation of the chip. The second fibre presents large amounts of damage being almost totally crushed by the round tool cutting edge. The third fibre, located near the EHM phase, shows damages mostly in the upper part. Damages in the matrix (Figure 17(b)) are more spread out, reaching the EHM phase.

The SPH model shows larger damaged areas both for fibre and matrix phases compared to the FEM model (Figure 6).

The equivalent plastic strain (i.e. the amount of permanent/non recoverable strain accumulated during machining) calculated in the subroutine for the matrix was stored in the solution-dependent state variable SDV7 and shown in Figure 18(a). A scale with a minimum value of 1.0e-3 has been set, while a maximum value of 0.32 has been considered. The latter represents the value of the plastic deformation at the onset of damage. Hence, all areas coloured in Figure 18(a) represent zones where no damage has been experienced yet. Instead, grey areas represent damaged material, where very large plastic deformation can occur. The magnitude of the plastic deformations reduces, moving far from the tool and showing values near to the maximum set around the damaged area, indicating imminent degradation of material properties. Plastic deformations rise in the matrix ahead of the tool and deep in the material reaching the EHM phase ($\sim$12 μm below the cutting plane). This behaviour represents a big difference to that observed in

the FEM model, where plastic deformations in the matrix remain contained around the cutting area, as shown in Figure 18(b). It is due to the presence of damaged material that, reaming in the SPH model, causes a bigger amount of material involved during cutting.

Fibre orientation θ=45°. The model configuration at the end of the analysis is reported in Figure 19. At the beginning of the analysis, the tool pushes the material along the cutting direction, causing damage in the particles in contact with the cutting edge. During tool advancement, material experiences shear with fibres undergoing displacement along their axis. Due to this behaviour, shear damage takes place in the weaker phase, the matrix. Further tool displacement causes an increase in the shear damage and damage propagation in a direction orthogonal to the fibre axis from the cutting edge.

The amount of damage increases as the tool advances, with the material being divided into two parts: the upper, forming the chip through shear deformation sliding on the rake face; and the lower, undergoing compression below the tool. As for fibre angle θ=0°, bouncing back due to elastic recovery after the tool has passed is clearly visible in Figure 19, as the clearance face and the workpiece machined surface are in contact. In addition, chip formation through shear deformation is highly visible at the end of the analysis, showing the chip shape. In general, the chip formation mechanism seems similar to that observed for the FEM model (Figure 8). It is representative of Type III chip formation mechanism.

Material damage is shown in Figure 20, by means of variable SDV13.

Material forming the chip experiences damage due to shear and compression. The latter is exerted by the tool on the area in front of the cutting edge; the consequent damage is transported by the material in the chip and in the machined surface. Damage extends below the cutting plane ($\sim$24 μm), reaching also the vertical free edge of the workpiece, propagating along the border area between the matrix and fibres (Figure 20(a)).

Matrix damage extends ahead of the cutting tool, especially at the border with the fibres due to shear deformation. Moreover, subsurface damages can also be observed in Figure 20(b). The path of the damage in the matrix seems to be influenced by the presence of fibres, travelling around them deep in the workpiece. Damage depth in the matrix ($\sim$19 μm) is higher than that experienced in the FEM model (Figure 9(a)), where it remains very close to the cutting plane (a few micrometer).

During advancement, the tool comes into contact with different fibres

sequentially. For each of them damage firstly propagates in a direction orthogonal to the fibre axis, and then it extends along the fibre-matrix border mainly towards the free surface. Further advancement of the tool causes damage propagation within the fibre, as visible in Figure 20(c). As for the matrix, the extension of damage in the fibres is larger when the SPH method is employed. In fact, it extends $\sim$24 μm below the cutting plane in the SPH model, while in the FEM model it extends a few micrometer (Figure 8).

The equivalent plastic strain for the matrix is reported in Figure 21. Very high plastic deformations are located in the areas that have experienced damage. As observed for fibre angle θ=0°, plastic deformations are not contained near the tool and the cutting plane, but they reach the EHM phase, assuming values $\sim$1.0e-3 in its vicinity (Figure 21(a)). Plastic deformations are much more contained in the FEM model as shown in Figure 21(b).

Fibre orientation θ=90°. The model configuration at the end of the analysis is shown in Figure 22. The cutting tool advancement causes a fibre failure due to compression at the contact point. The damaged area extends all around the cutting edge. Afterwards, the fibre is divided into two parts, with the upper part being lifted while sliding on the tool rake face, and compressed against the next fibre. The lifting causes a shear deformation in the material during chip formation. It is possible to observe that the machined surface exhibits elastic recovery after the tool has passed. The chip formation mechanism is similar to that observed in the FEM model (Type IV).

Material damage during cutting is shown in Figure 23. Damage extends ahead of the tool and below the cutting path ($\sim$24 μm). In particular, it seems to propagate equally in all directions starting from the cutting edge in the matrix phase (Figure 23(b)). This behaviour produces a damaged area having a circular shape around the tool. Damage extension is less expanded in the fibre phase (Figure 23(a)). Damage below the trim plane can be observed with the damage propagating along the fibre direction near the fibre-matrix border. In Figure 22(a) and Figure 23(a) it is also possible to notice as the first fibre, undergoing the cut, experiences a bending deformation in the opposite direction to the tool velocity. In fact, the tool compresses the fibres causing a bending deformation in the same direction as its displacement. After the fibre is cut, the lower part experiences an elastic recovery, which causes a fibre oscillation around the vertical position and an increase in the material damage. In fact, while the first fibre experiences the elastic recovery,

the second one is pushed forward by the tool. This double action causes further damage propagation in the machined material near the fibre-matrix boarder. Similar to the previous fibre orientations analysed, the damaged area is greater for the SPH model.

The equivalent plastic strain in the matrix phase has been reported in Figure 24. The plastic deformation experienced by the matrix is more extended in the SPH model. In fact, the particles having a grey colour in Figure 24(a) represent damaged areas, below which plastic deformation is visible. It reduces in magnitude moving away from the tool, deep in the workpiece. Differently, in the FEM model the plastic deformation is more contained near the tool, Figure 24(b).

Fibre orientation θ=135°. The model configuration is reported in Figure 25. Material removal can be studied observing material deformation during cutting combined with damage experienced by the material; these are reported in Figure 26 and Figure 27. During advancement the tool engages the fibre, exerting a peeling action while pushing forward (Figure 26). This causes a bending deformation of the fibre with local compression at the contact point with the cutting edge. The former causes separation between the fibre and the matrix below the cutting plane; while the latter causes a fibre fracture. Bending deformation is experienced by numerous fibres ahead of the tool, with damage rising far ahead of the tool at the border between the fibre and matrix. A further displacement of the tool causes a fibre failure due to bending, with the upper part fractured into two pieces due to compression. Similar behaviour is experienced by the following fibre which undergoes bending and compression. The upper parts of fractured fibres fly away in the form of a powder-like chip. The border of the damaged area ahead of the tool extends in a direction orthogonal to the fibre orientation, towards the free surface of the workpiece.

Despite the SPH method not implementing cohesive elements, it is able to predict the fibre-matrix detachment due to the failure of particles near the border along the fibre direction. This behaviour, which can be observed in Figure 27, may be interpreted as debonding.

In order to observe a periodic chip formation, a bigger cutting length should be simulated. However, the model seems to predict a chip formation mechanism similar to Type V in agreement with the literature [3].

The equivalent plastic strain in the matrix phase is reported in Figure 28(a) and compared with that obtained in the FEM results (Figure 28(b)).

As for previous orientations, the area affected by plastic deformation during cutting is more extended in the SPH model, propagating along the fibre direction. The particles in grey represent the damaged material, which is surrounded by elements where the damage is imminent. Plastic deformation reduces, moving far from the cutting zone.

Since in the FEM model elements are deleted during the analysis, plastic deformation and damage are contained, compared with the SPH model. In fact, when an element is deleted, the tool moves forward until it comes into contact with the next element. Differently, in the SPH method the damaged material is still present in the model, interposing between tool and the undamaged material. No loss of contact is generally visible between the tool and the workpiece. It generates larger areas of damage and deformation increasing the volume of material involved during cutting.

4.2. Type and morphology of the chip

The chip obtained using the SPH method was compared with that observed with the FEM method and also with experimental published data (Figure 29). For the latter, images obtained by Calzada *et al.* [16], using a high-speed camera, were considered.

Chips obtained from experiments seem to be continuous for all fibre orientations, except for θ=135°. For fibre angle θ=0°, a big difference can be noticed between the SPH and the FEM results. Even if the former produces a discontinuous chip, formed by short fibre pieces due to bending failure, the chip formation mechanism is more similar to that observed in the experiments (Type I). Differently, in the FEM model the element deletion due to failure causes non physical behaviour with material loss during cutting.

Independently on fibre orientation, the FEM model usually generates a fragmented chip, which is formed by isolated fibre pieces with a few matrix elements attached to them. On the macro-scale it can be described as a powder-like chip. In contrast, the chip formed using the SPH method is continuous for fibre angles θ=45° and θ=90°, as observed in the experiments. It is composed mainly of damaged particles, which can interact between each other after failure, deforming according to the constitutive model implemented in the VUMAT subroutine.

When machining at θ=90° using the SPH method, the chip sliding on the rake face tends to separate from the tool, forming a curling chip. This behaviour is comparable with the high-speed camera image. It is less visible for fibre orientation θ=45°.

Fibre angle θ=135° represents the most expensive numerical model. It is due to the large number of elements necessary to represent the composite material for that fibre orientation. For this reason, only the cutting length necessary to study and understand the chip formation mechanism was simulated. It is not enough to observe the formation of the periodic chip, differently by the other orientations. However, using the SPH model, fibres are able to withstand higher bending deformations. Even in this case, the FEM model generates a chip formed by separated short fibres. The SPH method seems more prone to show a deformation similar to the experimental image, where fibres deform in a bundle, remaining connected to each other.

4.3. Bouncing back

The bouncing back represents the amount of elastic recovery the workpiece undergoes after the tool has passed, which influences the depth of cut and the thrust force. The bouncing back can be observed and studied when using the SPH method, differently from the FEM method where the element deletion usually leads to a gap between the tool clearance face and the machined surface. Hence, the magnitude of the elastic recovery the material undergoes can be measured for the SPH method at each fibre orientation. Values obtained are reported in Figure 30. It is possible to observe that the predicted bouncing back amount decreases with fibre orientation. This is in contrast with experimental results obtained by Wang and Zhang [31], where the bouncing back was observed to be about the cutting edge radius for θ<90°, while it can reach more than double of the tool radius for θ>90°. This can be justified considering the simulated cutting length. It represents an important factor that could affect the measurements. In fact, after the tool has passed the material needs time to experience the elastic recovery. Hence, a long cutting length is required to move the tool far from the machined area, where the bouncing back is measured, allowing the material to reach the final configuration. Except for fibre orientation θ=0°, material elastic recovery was not totally completed at the end of the analysis. In addition, chip formation was not completed during simulation at fibre angle θ=135°, due to the high computational cost. For this reason only the bouncing back at fibre orientation θ=0° can be considered for discussion. It is shown in Figure 31. The bouncing back amount was estimated to be about $\sim$5 μm, i.e. equal to the cutting edge radius of the tool, which represents the expected value based on the experimental observation of Wang and Zhang [31]. This result highlighted the ability of the SPH method to provide additional

and important information when compared to the FEM, and to consider the effects of the bouncing back on the actual depth of cut and the thrust force during cutting. In fact, it is possible to assert that for fibre orientation θ=0°, the nominal depth of cut is 15 μm, but due to the bouncing back the real (actual) depth of cut is 10 μm. Consequently, the thrust force is affected by the elastic recovery of the material that pushing against the clearance face of the tool generates a force component along a direction orthogonal to the cutting speed and directed upwards.

Prediction of bouncing back using SPH method can be further improved optimising the damage variables for matrix and fibres by means of an iterative approach aiming to minimise discrepancies with expected results.

4.4. Cutting force and thrust force

Cutting force and thrust force calculated in the SPH model were compared with results obtained by means of a FEM model and from experiments [16].

Cutting force prediction improves when using the SPH method, except for fibre orientation θ=135° (Figure 32). In particular, a good agreement can be observed for θ=0° and θ=90°, with an improvement of 31% and 4.3% compared with FEM model, respectively. Cutting force at θ=45° remains underestimated with an error of ∼27 %. At fibre angle θ=135°, both the SPH model and the FEM model overestimate the cutting force, with the former showing a prediction which is double of the experimental value. This could be attributed to the cutting length simulated, which is not sufficient to observe a periodic chip, and so it is not really representative of the average cutting force during machining.

The SPH method shows a better agreement with the experimental results in terms of thrust force for all the fibre orientations considered (Figure 33). It is possible to observe a large increase in the force predicted compared to the FEM model, becoming closer to the experimental results. It is particularly evident for fibre angles θ=0°,90°,135°, where prediction improve of 26%, 29.7% and 28%, respectively. However, thrust force is still underestimated for all fibre angles.

Since bouncing back and thrust force are connected, a longer analysis time could increase the thrust force due to an increase of the bouncing back, allowing the material to reach the final configuration after the tool has passed.

Prediction of machining force using SPH method can be further improved optimising the damage variables for matrix and fibres by means of an iterative

approach aiming to minimise discrepancies with experimental results.

5. Conclusions

The smoothed particle hydrodynamics method has been employed to simulate the orthogonal cutting of UD-CFRP, using the micro-mechanical approach. Different fibre orientations have been considered and results compared with those obtained using a FE method and against experimental findings [16].

The SPH method has proved to be more capable in simulating the chip formation mechanisms, especially at fibre orientation θ=0°, providing also detailed information on the bouncing back and consequently on the real depth of cut. In particular, for fibre orientation θ=0° the cutting length simulated is enough to measure the final bouncing back amount. It has been found to be equal to the cutting edge radius ($\sim$5 μm), as expected from the literature, and leading to a real (actual) depth of cut of 10 μm starting from a nominal depth of cut of 15 μm.

For all fibre orientations damage extension is larger when employing the SPH method due to the presence of damaged material around the tool, which causes an increase of material involved in the cutting. For the same reason, also the matrix' plastic deformation in the machined workpiece results more extended.

In general, the chip morphology predicted by the SPH method seems to be more accurate when compared with high-speed camera images, being more prone to generate a continuous chip. In addition, for θ=0° and θ=135°, it is possible to observe how the SPH method is able to predict behaviour similar to debonding at the fibre-matrix border.

The SPH method shows also a better prediction in terms of cutting force for all fibre orientations, except for θ=135°. Improvements can reach $\sim$30% for θ=0°. The high value presented for θ=135° can be associated with the cutting length simulated, which is not enough to obtain a periodic chip and so a reliable value for the average cutting force. Thrust force results improve using the SPH method for all fibre orientations reaching $\sim$30% improvement for θ=90° and θ=135°, and $\sim$26% for θ=0°compared to the FE method. However, a longer cutting length could help in increasing the numerical thrust force bringing them closer to the experimental values due to an increase of bouncing back (increase of material pushing of the tool clearance face due to elastic recovery).

Finally, it is possible to assert that the SPH method is able to improve the prediction of chip formation mechanisms and machining force during cutting compared with the generally used FE method, allowing also studying the bouncing back, hence providing a prediction of the actual depth of cut. However, differently from the FE method it is not able to provide any information on the fibre-matrix interface due to the absence of a cohesive model.

Numerical results using SPH method can be further improved optimising the damage variables for matrix and fibres by means of an iterative approach aiming to minimise discrepancies with experimental results.

References

[1] A. Abena, Advanced modelling for the orthogonal cutting of unidirectional carbon fibre reinforced plastic composites, Ph.D. thesis, 2017.

[2] D. Wang, M. Ramulu, D. Arola, Orthogonal cutting mechanisms of graphite/epoxy composite. Part I: Unidirectional laminate, Int J Mach Tools Manufact 35 (12) (1995) 1623–1638.

[3] J. Y. Sheikh-Ahmad, Machining of polymer composites, Springer Science+Business Media, 2009.

[4] H. Pwu, H. Hocheng, Chip formation model of cutting fiber-reinforced plastics perpendicular to fiber axis, J Manuf Sci E 120 (1998) 192–196.

[5] K. Chawla, Composite material:science and engineering, Springer Science+Business Media, 2012.

[6] G. V. G. Rao, P. Mahajan, N. Bhatnagar, Three-dimensional macromechanical finite element model for machining of unidirectional-fiber reinforced polymer composites, Mat Sci Eng A 498 (2008) 142–149.

[7] J. L. Cantero, C. Santiuste, N. Marín, X. Soldani, H. Miguélez, 2D and 3D approaches to simulation of metal and composite cutting, in: AIP Conference Proceedings, vol. 1431, AIP Publishing, 651–659, 2012.

[8] C. Santiuste, A. Olmedo, X. Soldani, H. Miguélez, Delamination prediction in orthogonal machining of carbon long fiber-reinforced polymer composites, J Reinf Plast Compos 31 (2012) 875–885.

[9] C. Santiuste, X. Soldani, M. Miguélez, Machining FEM model of long fiber composites for aeronautical components, Compos Struct 92 (2010) 691–698.

[10] D. Nayak, I. Singh, N. Bhatnagar, P. Mahajan, An analysis of machining induced ddamage in FRP composites - a micromechanics finite element approach, AIP Conf Proc 712 (2004) 327–331.

[11] C. Dandekar, Y. Shin, Multiphase finite element modeling of machining unidirectional composites: prediction of debonding and fiber damage, J Manuf Sci E 130 (2008) 1–12.

[12] D. Iliescu, D. Gehin, I. Iordanoff, F. Girot, M. Guetiérrez, A discrete element method for the simulation of CFRP cutting, Compos Sci Technol 70 (2010) 73–80.

[13] V. Palani, Finite element simulation of 3D drilling in unidirectional CFRP composite, Master's thesis, Wichita State University, 2006.

[14] O. Isbilir, E. Ghassemieh, Numerical investigation of the effects of drill geometry on drilling induced delamination of carbon fiber reinforced composites, Compos Struct 105 (2013) 126–133.

[15] V. Phadnis, A. Roy, V. Silberschmidt, A finite element model of ultrasonically assisted drilling in carbon/epoxy composites, Procedia CIRP 8 (2013) 141–146.

[16] K. A. Calzada, S. G. Kapoor, R. E. D. Vor, J. Samuel, A. K. Srivastava, Modeling and interpretation of fiber orientation-based failure mechanisms in machining of carbon fiber-reinforced composites, J Manuf Proces 14 (2012) 141–149.

[17] G. V. G. Rao, P. Mahajan, N. Bhatnagar, Micro-mechanical modeling of machining of FRP composites - cutting force analysis, Compos Sci Technol 67 (2007) 579–593.

[18] G. V. G. Rao, P. Mahajan, N. Bhatnagar, Machining of UD-GFRP composites chip formation mechanism, Compos Sci Technol 67 (2007) 2271–2281.

[19] R. Rentsch, O. Pecat, E. Brinksmeier, Macro and micro process modeling of the cutting of carbon fiber reinforced plastics using FEM, Procedia Eng 10 (2011) 1823–1828.

[20] A. Abena, S. Soo, K. Essa, Modelling the orthogonal cutting of UD-CFRP composites: Development of a novel cohesive zone model, Compos Struct 168 (2017) 65–83.

[21] G. Chennakesavelu, Orthogonal machining of uni-directional carbon fiber reinforced polymer composites, Master's thesis, Golden Valley Institute of Technology, 2006.

[22] X. Weixing, L. C. Zhang, Y. Wu, Elliptic vibration-assisted cutting of fibre-reinforced polymer composites: Understanding the material removal mechanisms, Compos Sci Technol 92 (2014) 103–111.

[23] W. Tang, Y. Chen, H. Yang, Numerical investigation of delamination in drilling of carbon fiber reinforced polymer composites, Appl Compos Mater (2018) 1–21.

[24] A. Abena, S. Soo, K. Essa, A finite element simulation for orthogonal cutting of UD-CFRP incorporating a novel fibre-matrix interface model, Procedia CIRP 31 (2015) 539–544.

[25] A. Zahedi, S. Li, A. Roy, V. Babitsky, V. Silberschmidt, Application of Smooth-Particle Hydrodynamics in metal machining, J Phys: Conf Ser 382 (2012) 12–17.

[26] F. Spreng, P. Eberhard, Machining process simulations with smoothed particle hydrodynamics, Procedia CIRP 31 (2015) 94–99.

[27] M. Madaj, M. Píška, On the SPH Orthogonal cutting simulation of A2024-T351 alloy, Procedia CIRP 8 (2013) 152–157.

[28] M. Zetterberg, A critical overview of machining simulations in ABAQUS, Master's thesis, KTH Royal Institute Of Technology, 2014.

[29] J. Limido, C. Espinosa, M. Salaün, C. Mabru, R. Chieragatti, High speed machining modelling: SPH method capabilities, 4th SPHERIC .

[30] J. Limido, C. Espinosa, M. Salaün, J. Lacome, SPH mothod applied to high speed cuttign modelling, Int J Mech Sci 49 (2007) 898–908.

[31] X. Wang, L. Zhang, An experiemental investigation into the orthogonal cutting of unidirectional fibre reinforced plastics, Int J Mach Tools Manufact 43 (2003) 1015–1022.

[32] ABAQUS User 's Manual, version 6.13 .

[33] I. Kanpur, P. Mohite, Composite materials and structures, NPTEL, URL https://nptel.ac.in/courses/101104010/.

[34] L. Iannucci, J. Ankersen, An energy based damage model for thin laminated composites, Compos Sci Technol 66 (2006) 934–951.

[35] D. Arola, M. Ramulu, D. Wang, Chip formation in the orthogonal trimming of graphite/epoxy composite, Composites Part A 27A (1996) 121–133.

[36] M. Ramulu, Machining and surface integrity of fibre-reinforced plastic composites, SADHANA-ACAD P ENG S 22 (1997) 449–472.

[37] H. Li, X. Qin, G. He, Y. Gin, D. Sun, M. Prince, Investigation of chip formation and fracture toughness in orthogonal cutting of UD-CFRP, Int Adv Manuf Technol 82 (2016) 1079–1088.

[38] P. P. Camanho, C. Davila, Mixed-mode dechoesion finite elements for the simulation of delamination in composite materials, Tech. Rep. NASA/TM-2002-211737, National Aeronautics and Space Administration (NASA), 2002.

[39] J. Littell, C. Ruggeri, R. Goldberg, G. Roberts, W. Arnold, W. Binienda, Measurement of epoxy resin tension, compression, shear stress-strain curves over a wide range of strain rrate using small test specimens, J Aerosp Eng 21 (2008) 162–173.

Table 1: Material properties for carbon fibre, epoxy matrix, fibre-matrix interface and EHM phase implemented in the numerical model [16, 17, 38, 39].

Material	Property	Value
Carbon fibre	Elastic constants	E_1=235 GPa, E_2=E_3=14 GPa
		$\nu_{12} = \nu_{13}$=0.2, ν_{23}=0.25
		G_{12}=G_{13}=28 GPa, G_{23}=5.5 GPa
	Longitudinal strength	X_t=3.59 GPa, X_c=3 GPa
	Diameter	7.5 μm
	Volume percentage	60 %
Epoxy	Elastic constants	E=2.96 GPa, ν=0.4
	Yield strength	σ_y=74.7 MPa
Interface	Normal strength	σ_{max}=167.5 MPa
	Shear strength	τ_{max}=25 MPa
	Fracture energy	G^c=0.05 N/mm^2
EHM	Elastic constants	E_1=142.184 GPa, E_2=E_3=7.606 GPa
		$\nu_{12} = \nu_{13}$=0.28, ν_{23} ==0.347
		G_{12}=G_{13}=4.151 GPa, G_{23}=2.824 GPa

Table 2: Machining parameters [16].

Tool	5 μm edge radius
	10° clearance angle
	25° rake angle
Cutting speed	500 mm/min
Depth of cut	15 μm
Fibre orientations	0°, 45°, 90°, 135°

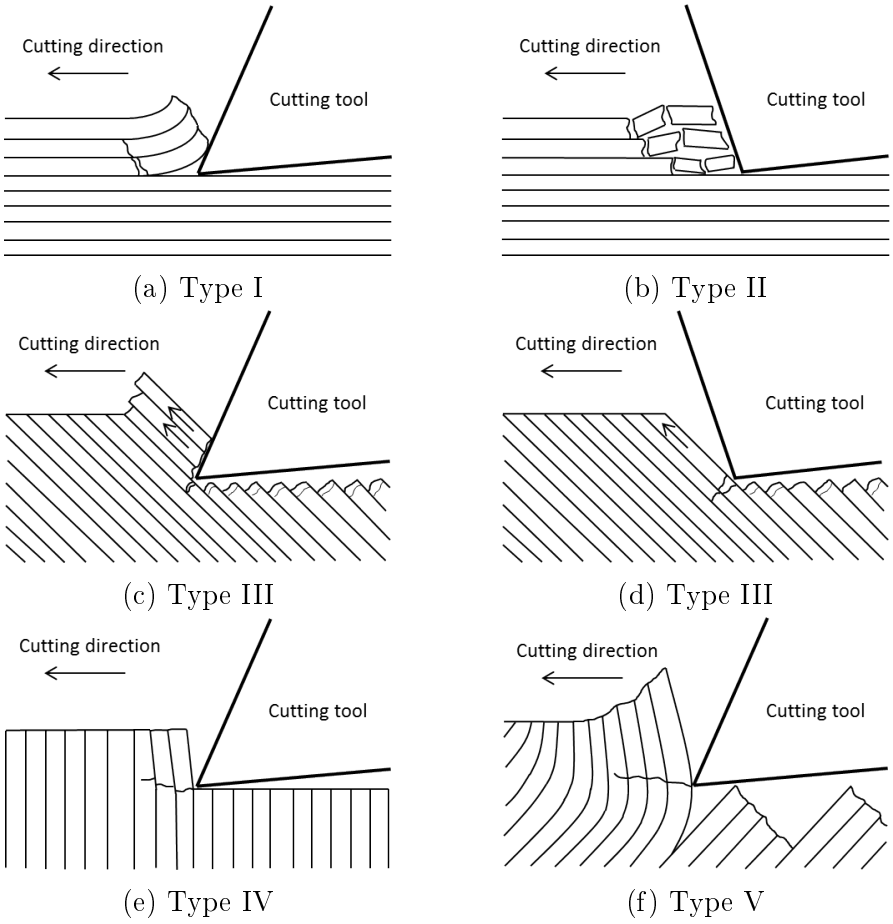

Figure 1: Influence of fibre orientation and tool rake angle on the chip formation mechanisms [2]: (a) θ=0°- α>0°; (b) θ=0°- α<0°; (c) θ=45°- α>0°; (d) θ=45°- α<0°; (e) θ=90°- α>0°; (f) θ=135°- α>0°.

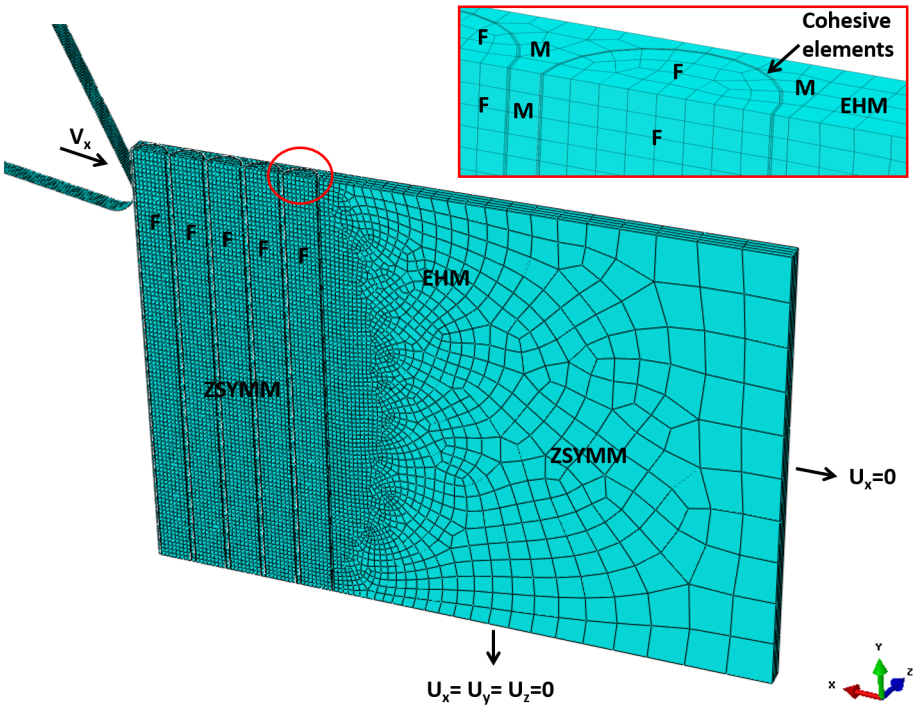

Figure 2: Schematic of the three-dimensional FEM model for fibre orientation θ=90° with applied boundary conditions.

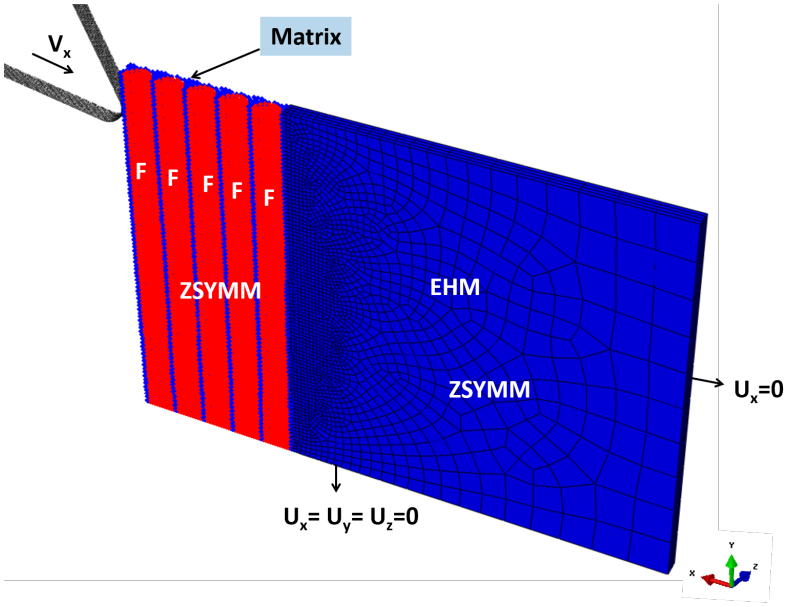

(a)

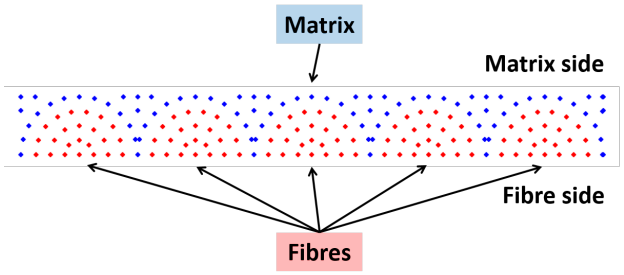

(b)

Figure 3: Schematic of the three-dimensional SPH model for fibre orientation θ=90°: (a) boundary conditions applied ; and (b) details of fibre and matrix (top view).

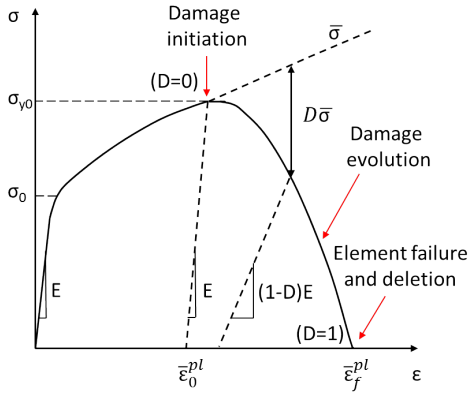

(a) Progressive damage degradation in Abaqus [32]

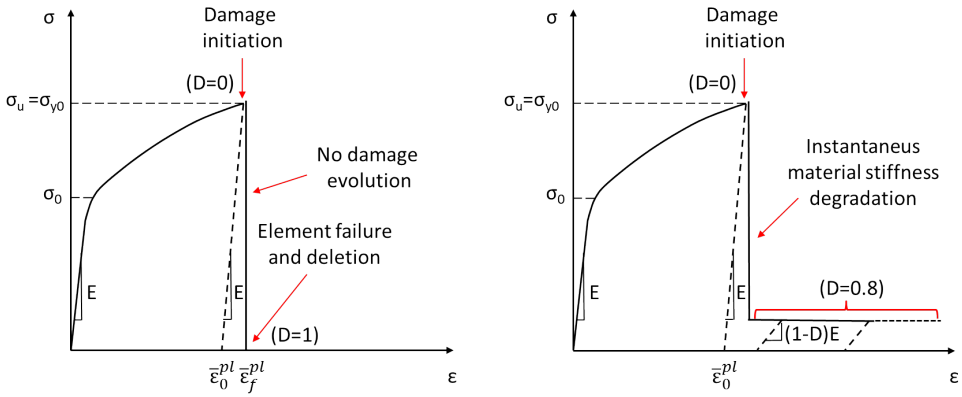

(b) FEM (c) SPH

Figure 4: Stress-strain curve considering damage during simulation.

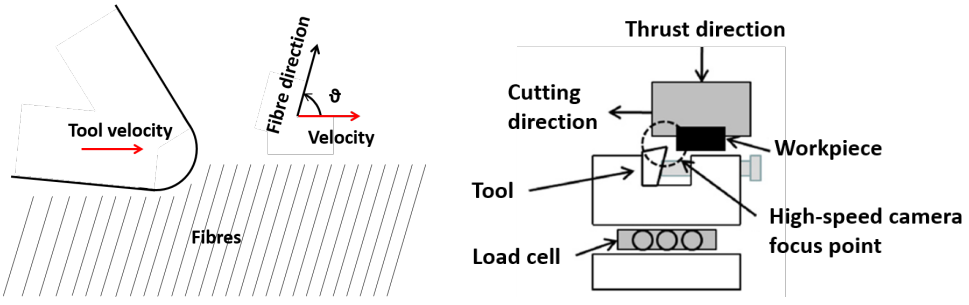

(a) (b)

Figure 5: (a) Fibre angle definition; and (b) schematic of the experimental setup for a micro-scale orthogonal cutting [16].

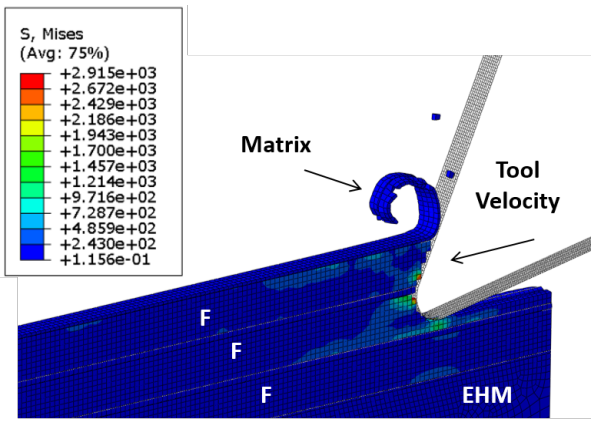

Figure 6: Model configuration during cutting for fibre orientation θ=0°.

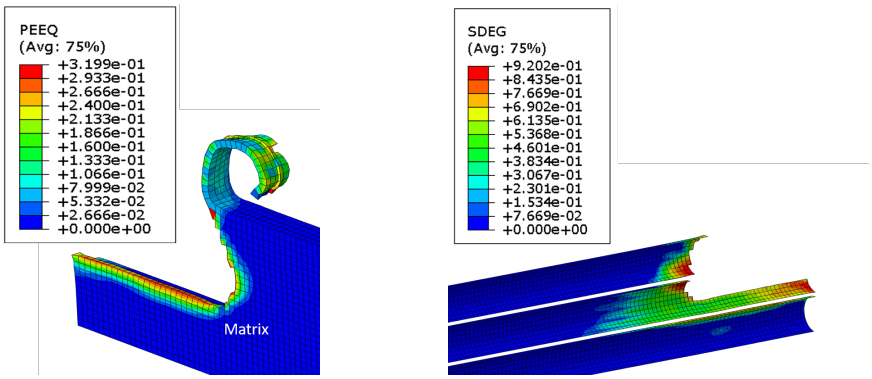

(a) Matrix (b) Cohesive zone

Figure 7: (a) Equivalent plastic strain in the matrix (fibres and cohesive elements are not displayed); and (b) overall value of scalar damage SDEG for cohesive elements at fibre orientation θ=0°.

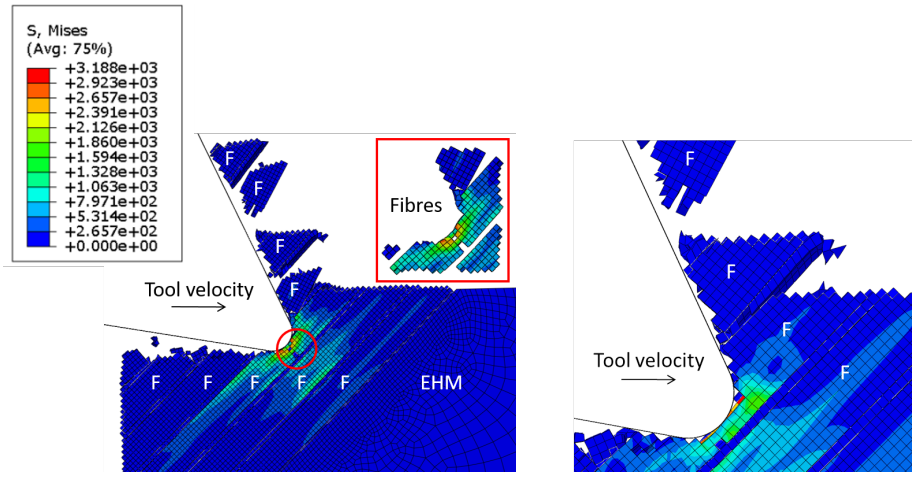

(a) (b)

Figure 8: (a) Model configuration during cutting; and (b) tool tip - workpiece interaction for fibre orientation θ=45°.

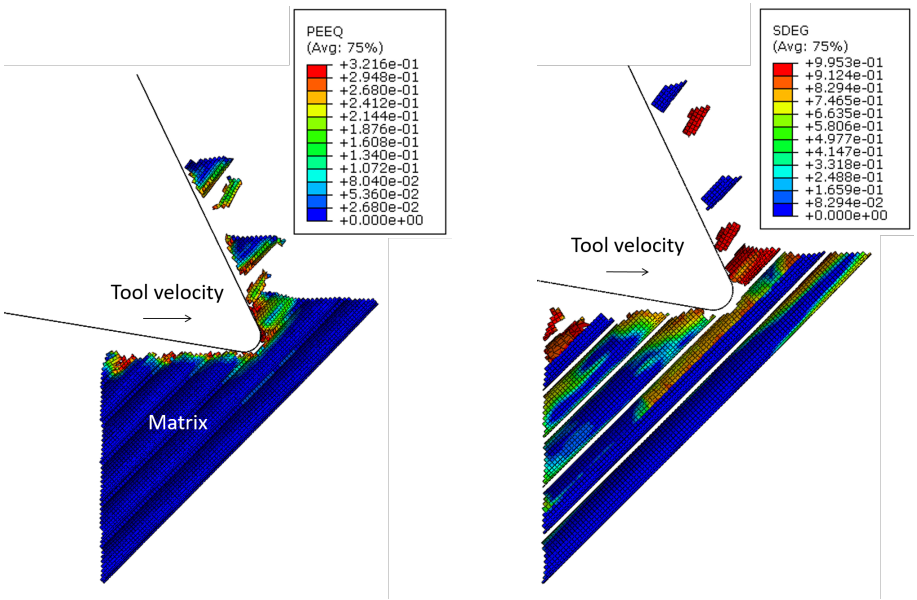

(a) Matrix (b) Cohesive zone

Figure 9: (a) Equivalent plastic strain in the matrix (fibres and cohesive elements are not displayed); and (b) overall value of scalar damage SDEG for cohesive elements at fibre orientation θ=45°.

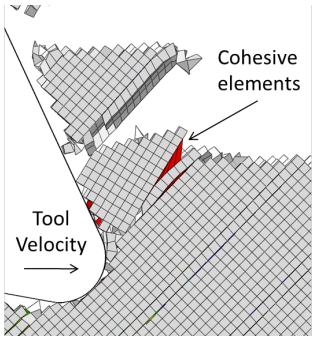

Figure 10: Cohesive elements' behaviour during cutting at fibre orientation θ=45°.

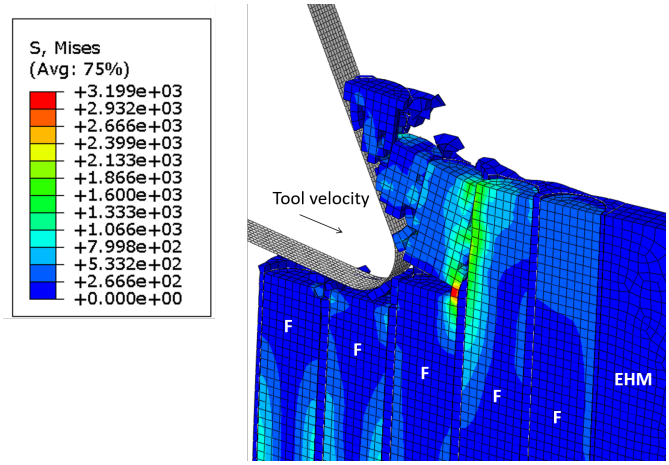

Figure 11: Model configuration during cutting for fibre orientation θ=90°.

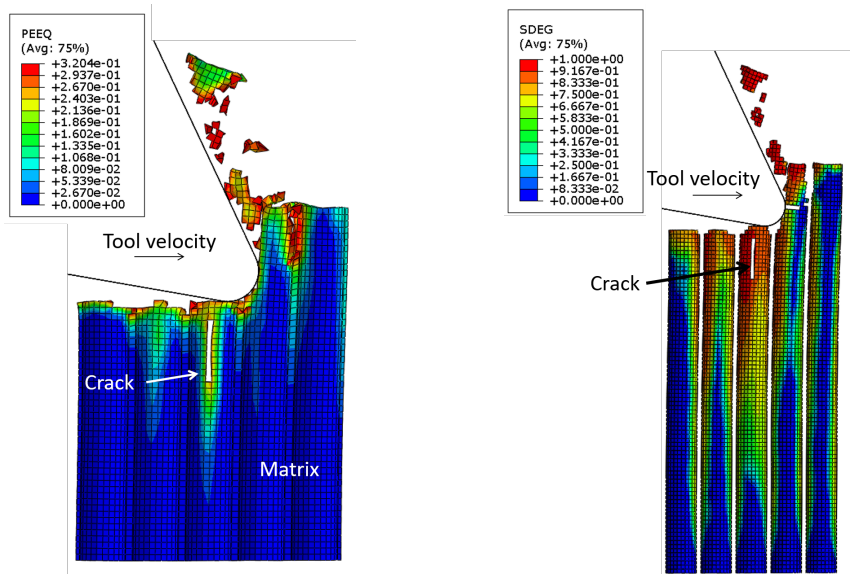

(a) Matrix (b) Cohesive zone

Figure 12: (a) Equivalent plastic strain in the matrix (fibres and cohesive elements are not displayed); and (b) overall value of scalar damage SDEG for cohesive elements at fibre orientation θ=90°.

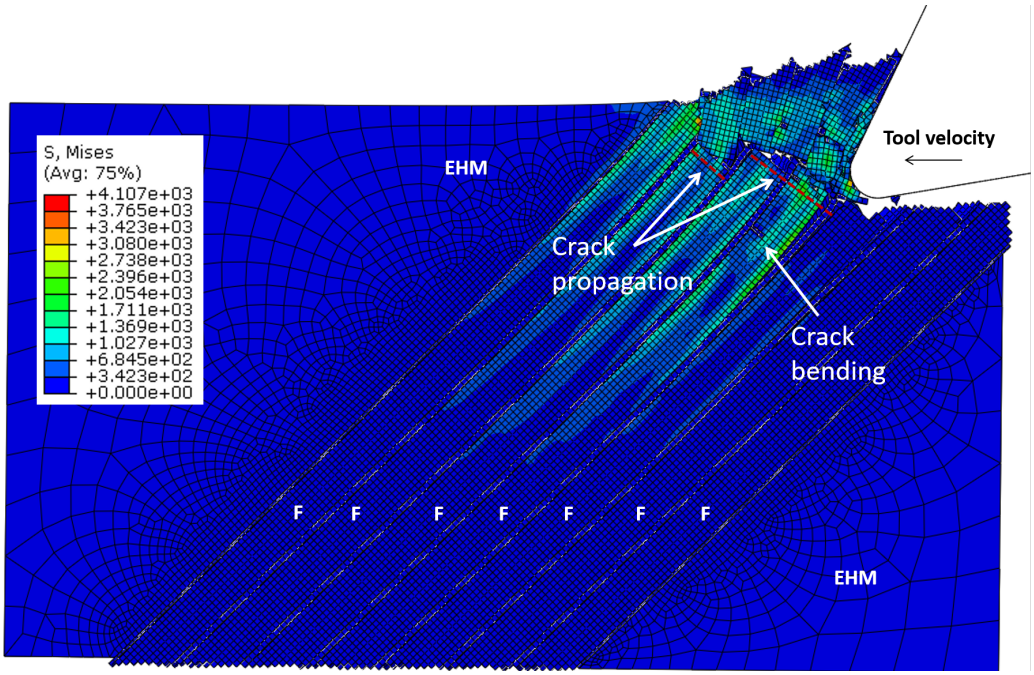

Figure 13: Model configuration during cutting for fibre orientation θ=135°.

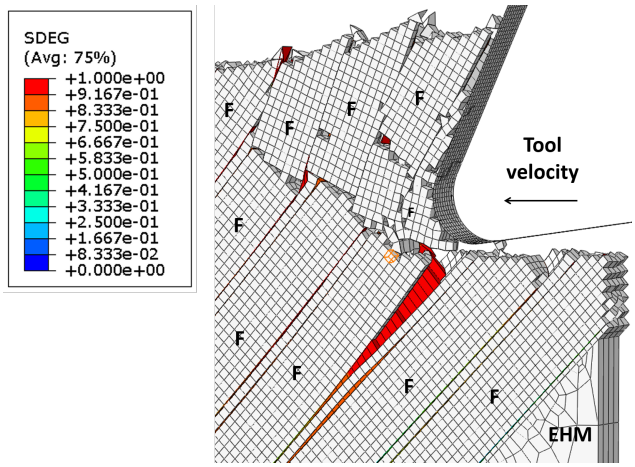

Figure 14: Debonding when machining at fibre orientation θ=135°.

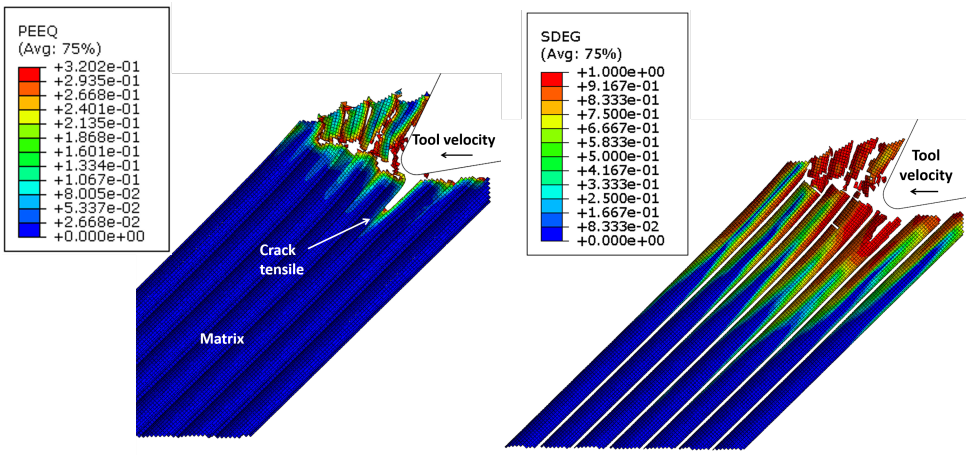

(a) Matrix (b) Cohesive zone

Figure 15: (a) Equivalent plastic strain in the matrix (fibres and cohesive elements are not displayed); and (b) overall value of scalar damage SDEG for cohesive elements at fibre orientation θ=135°.

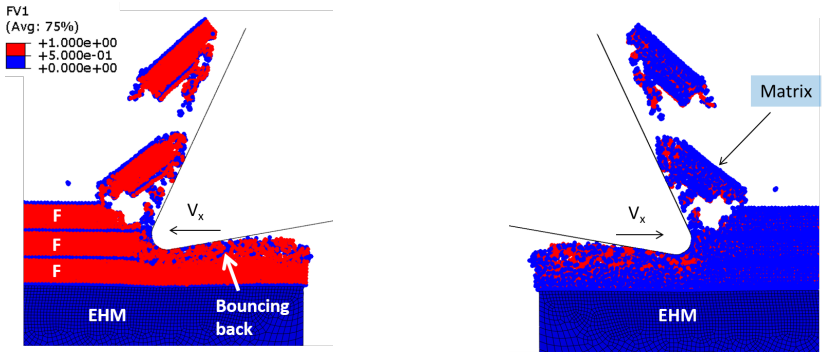

(a) Fibre side (b) Matrix side

Figure 16: Model configuration during cutting implementing the SPH method for fibre orientation θ=0°.

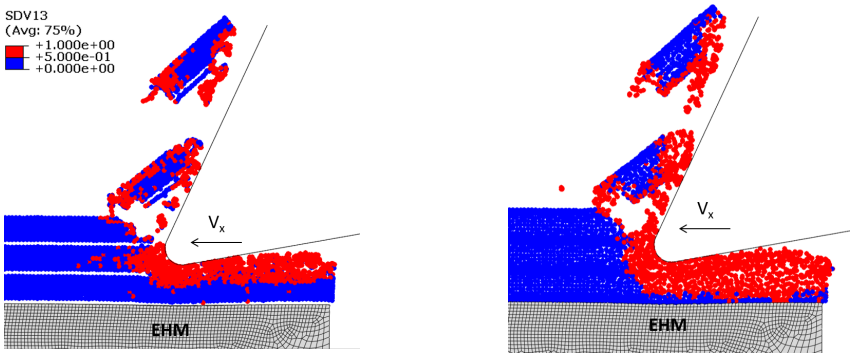

(a) Fibre damage (b) Matrix damage

Figure 17: Damage in (a) fibre and (b) matrix material identified by the variable SDV13 in the VUMAT subroutine for fibre orientation θ=0°.

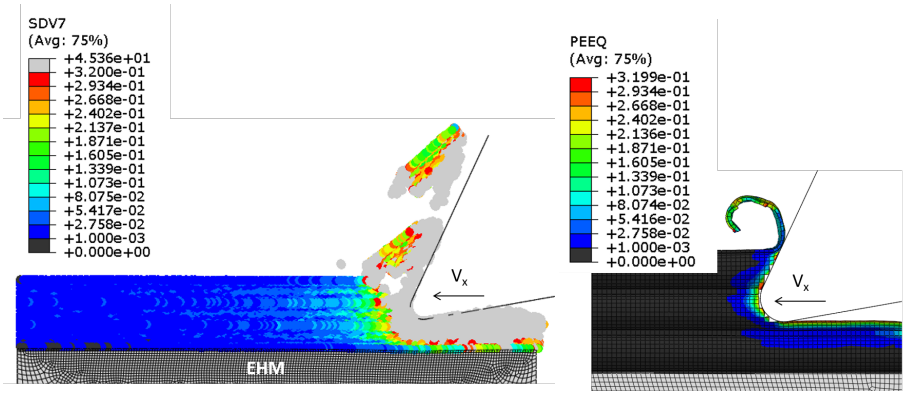

(a) SPH - Matrix (b) FEM - Matrix

Figure 18: Equivalent plastic strain in the matrix material for the (a) SPH model and the (b) FEM model at fibre orientation θ=0°.

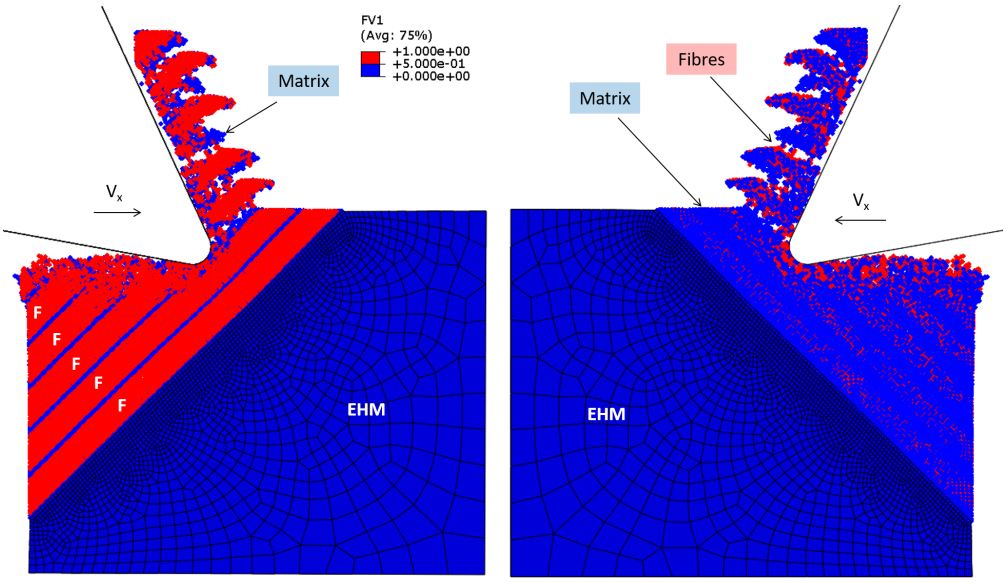

(a) Fibre side (b) Matrix side

Figure 19: Model configuration implementing the SPH method for fibre orientation θ=45°.

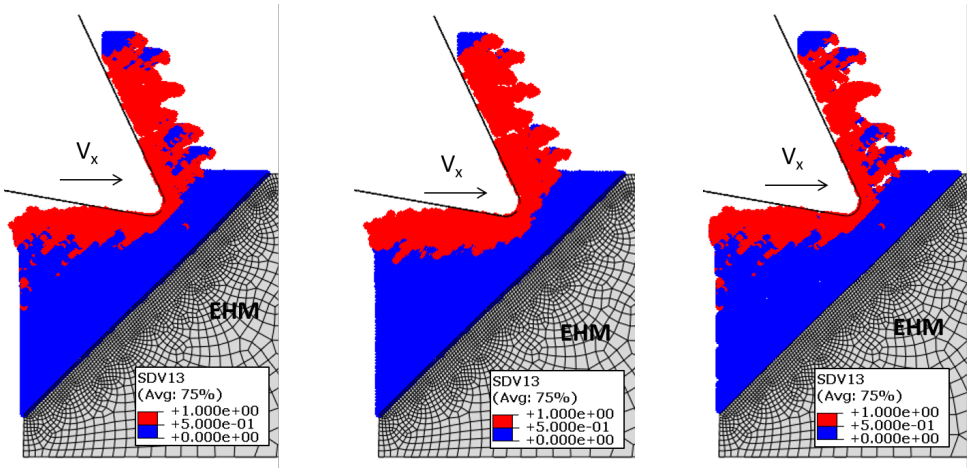

(a) Workpiece damage (b) Matrix damage (c) Fibre damage

Figure 20: Damage in (a) machined workpiece, (b) matrix material and (c) fibre material identified by the variable SDV13 in the VUMAT subroutine for fibre orientation θ=45°.

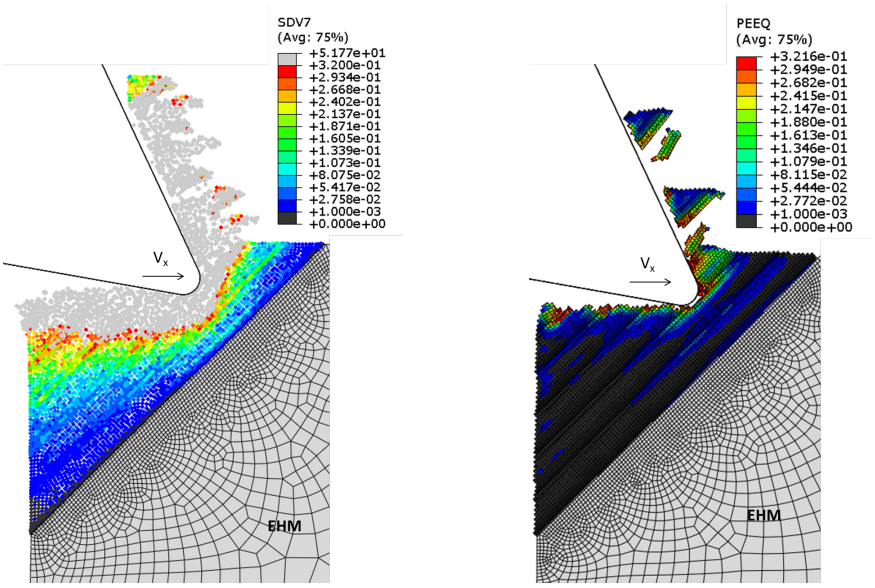

(a) SPH - Matrix (b) FEM - Matrix

Figure 21: Equivalent plastic strain in the matrix material for fibre orientation θ=45°.

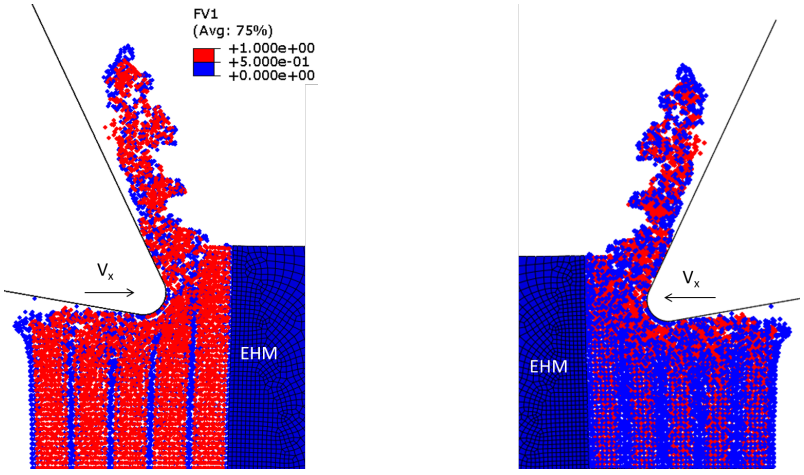

(a) Fibre side (b) Matrix side

Figure 22: Model configuration implementing the SPH method for fibre orientation θ=90°.

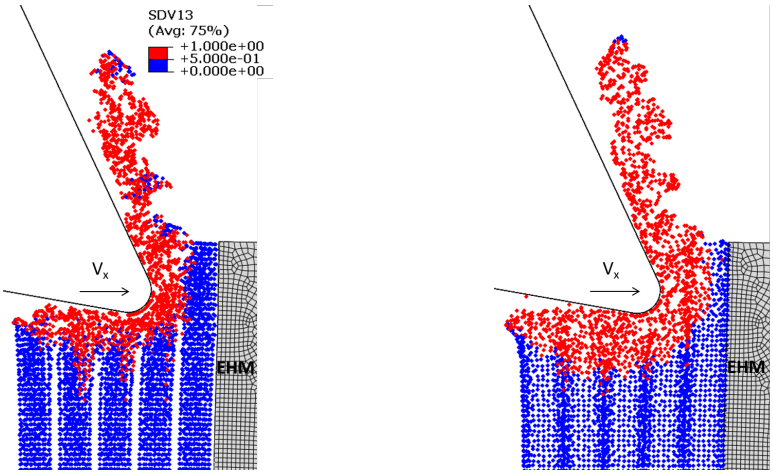

(a) Fibre damage (b) Matrix damage

Figure 23: Damage in (a) fibre and (b) matrix material identified by the variable SDV13 in the VUMAT subroutine for fibre orientation θ=90°.

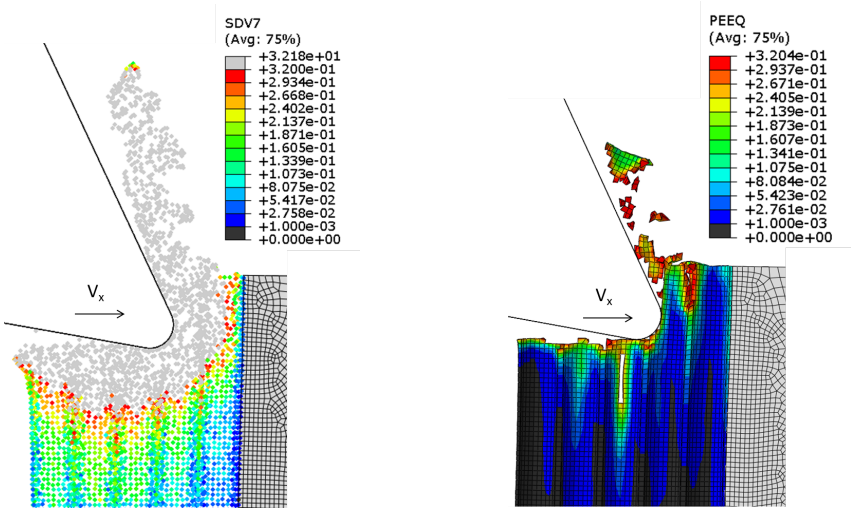

(a) SPH - Matrix (b) FEM - Matrix

Figure 24: Equivalent plastic strain in the matrix material for fibre orientation θ=90°.

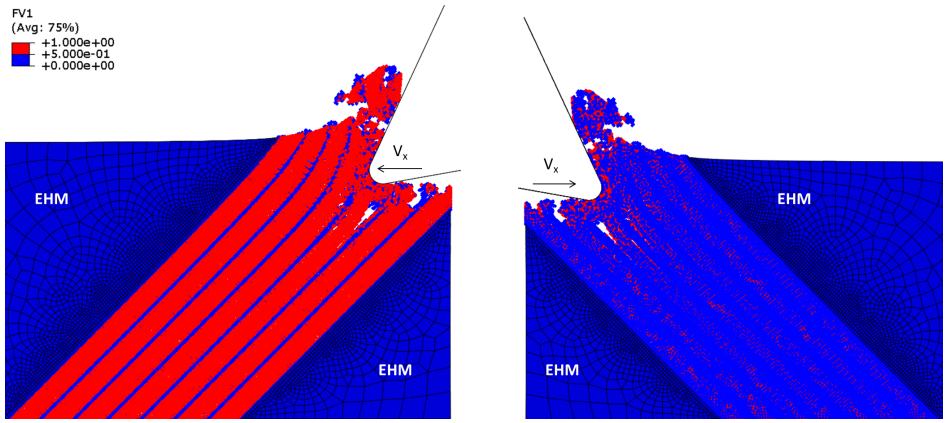

(a) Fibre side (b) Matrix side

Figure 25: Model configuration implementing the SPH method for fibre orientation θ=135°.

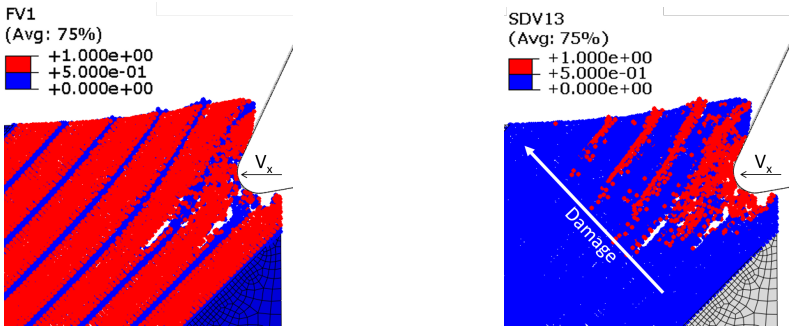

(a) FV1 - Fibre side (b) SDV13 - Fibre side

Figure 26: (a) Model configuration; and (b) damage at 1.97e-3 seconds for fibre orientation θ=135°.

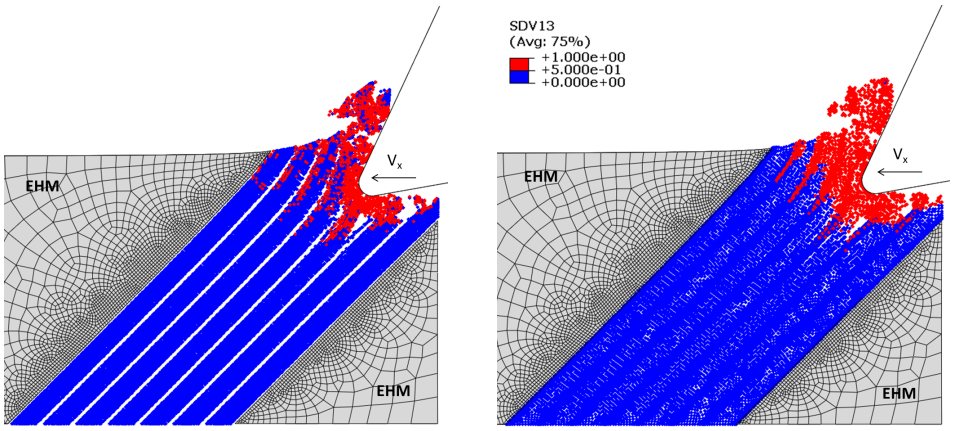

(a) Fibre damage (b) Matrix damage

Figure 27: Damage in (a) fibre and (b) matrix material identified by the variable SDV13 in the VUMAT subroutine for fibre orientation θ=135°.

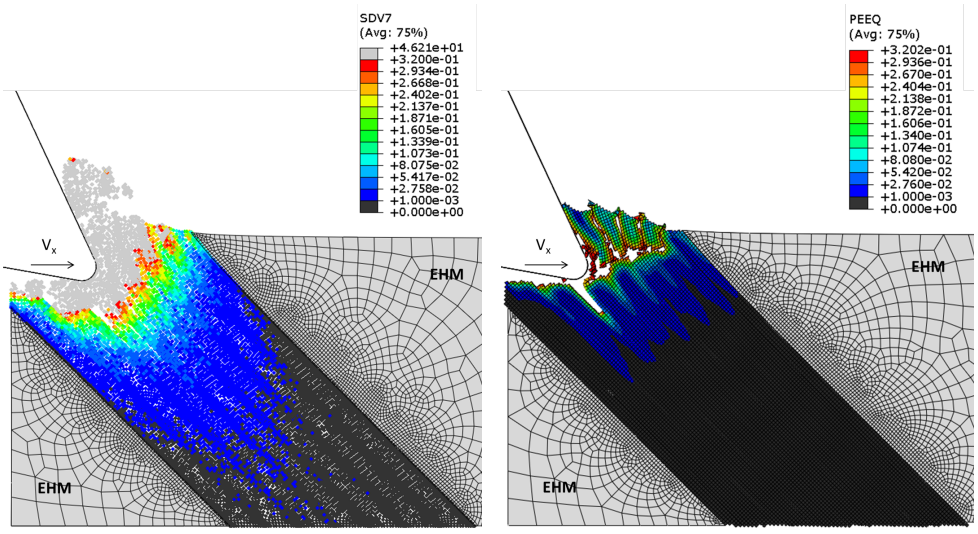

(a) SPH - Matrix (b) FEM - Matrix

Figure 28: Equivalent plastic strain in the matrix material for fibre orientation θ=135°.

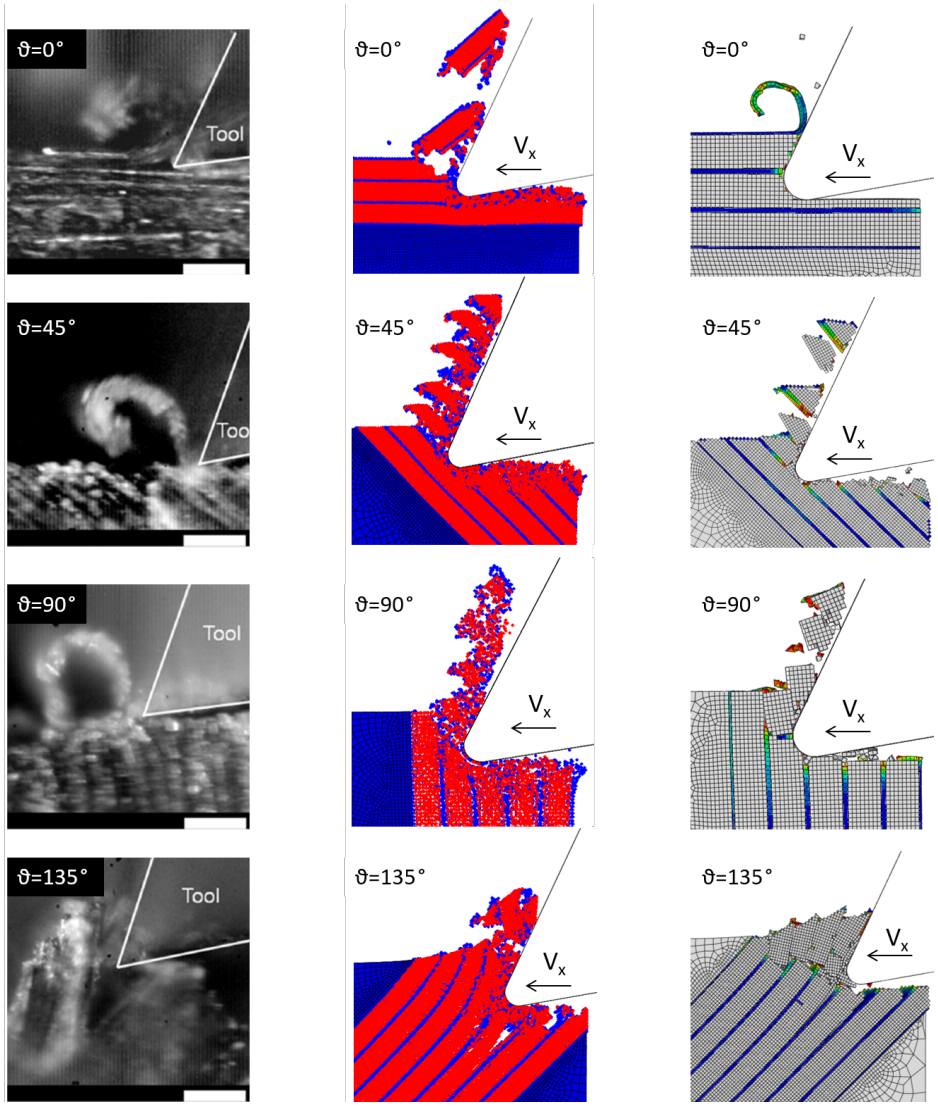

(a) Experiment (b) SPH (c) FEM

Figure 29: Comparison of chip morphology for different fibre orientations considering: (a) experimental results [16]; (b) SPH model; and (c) FEM model.

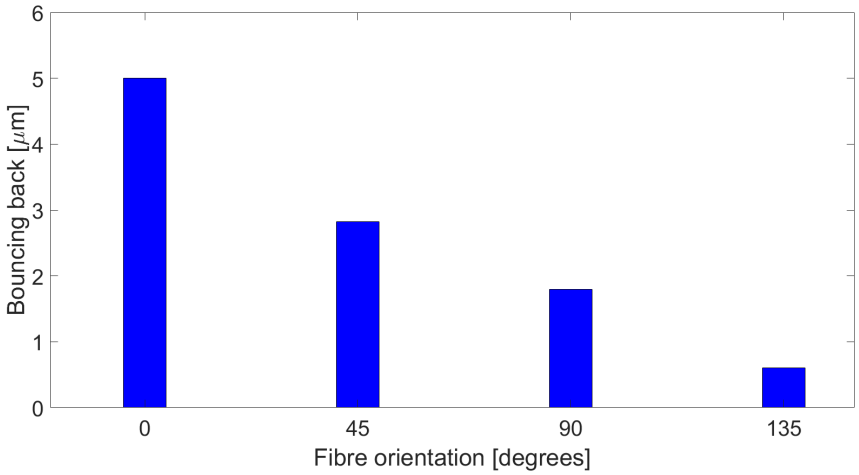

Figure 30: Bouncing back amount calculated when employing the SPH method for different fibre orientations.

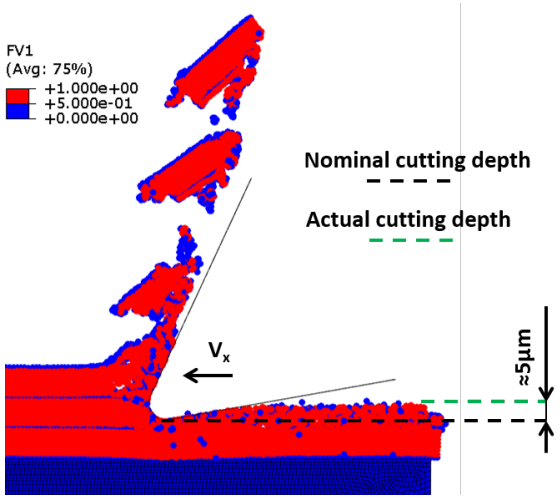

Figure 31: Bouncing back amount calculated when employing the SPH method at fibre orientation θ=0°.

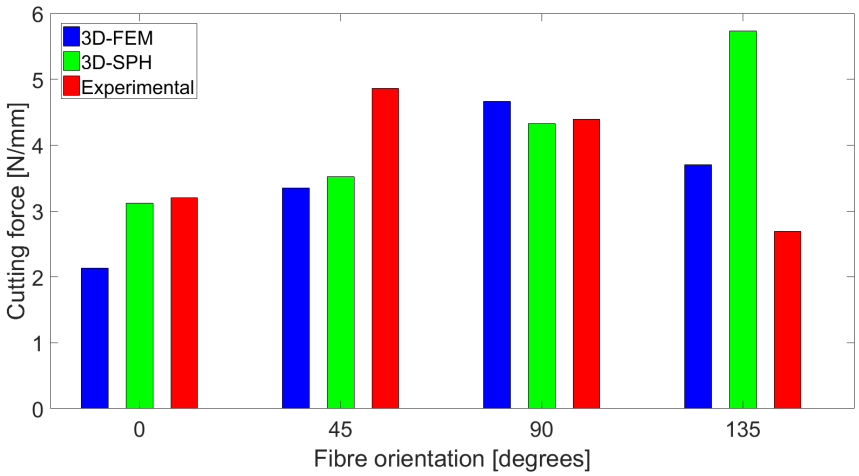

Figure 32: Cutting force comparison for the SPH model, FEM model, and experiments [16].

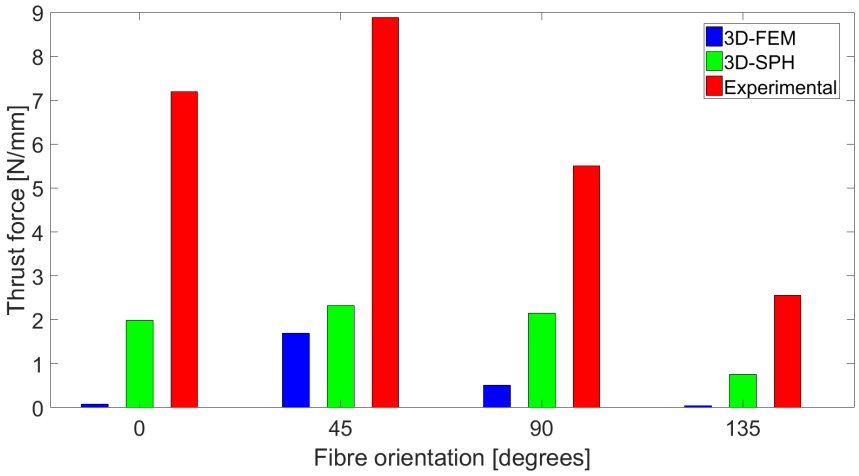

Figure 33: Thrust force comparison for the SPH model, FEM model, and experiments [16].